

Mapping of Functionalized Regions on Carbon Nanotubes by Scanning Tunneling Microscopy

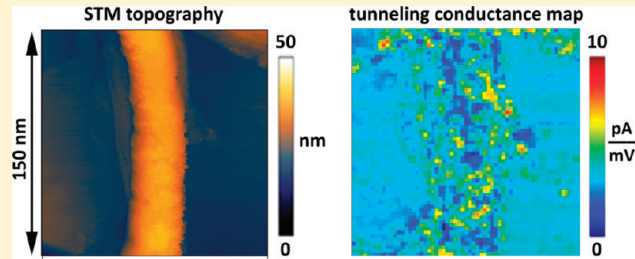
P. Nemes-Incze,^{*†} Z. Kónya,[‡] I. Kiricsi,[‡] Á. Pekker,[§] Z. E. Horváth,[†] K. Kamarás,[§] and L. P. Biró[†]

[†]Research Institute for Technical Physics and Materials Science, H-1525, P.O. Box 49, Budapest, Hungary

[‡]Department of Applied and Environmental Chemistry, University of Szeged, Rerrich Béla sqr. 1, H-6720 Szeged, Hungary

[§]Research Institute for Solid State Physics and Optics, Hungarian Academy of Sciences, H-1525, P.O. Box 49, Budapest, Hungary

ABSTRACT: Scanning tunneling microscopy gives us the opportunity to map the surface of functionalized carbon nanotubes in an energy resolved manner and with atomic precision. But this potential is largely untapped, mainly due to sample stability issues which inhibit reliable measurements. Here we present a simple and straightforward solution that makes away with this difficulty, by incorporating the functionalized multiwalled carbon nanotubes into a few-layer graphene–nanotube composite. This enabled us to measure energy resolved tunneling conductance maps on the nanotubes, which shed light on the level of doping and the dependence of defect creation or functionalization on crystallographic orientation.



INTRODUCTION

In the decades following their discovery, the chemistry of carbon nanotubes (CNTs) has grown into a mature field of research.^{1–3} Sidewall functionalization of CNTs has turned out to be a versatile tool to change their electronic properties^{4–7} and the ways in which the tubes interact with their environment.^{8–11} This considerably broadens their applicability, from sensors and medical uses^{2,10,12,13} to composite materials.⁸ In all such cases, we need a clear picture of the changes functionalization induces in the nanotube, such as surface topography, band structure, doping, etc., to be able to refine these applications and to better understand the physical and chemical processes involved in functionalization. Changes to the nanotube electronic structure are usually investigated by spectroscopy, which is a global probe of CNT properties.⁶ Complementary to these methods are scanning probe methods, namely, scanning tunneling microscopy (STM) and atomic force microscopy (AFM), which provide spatially resolved information down to the atomic scale. STM is one of the most important tools in nanoscale science and has been the source of landmark findings in the study of carbon nanotubes. Using STM, Wildöer et al. gave a first account of the relation between CNT chirality and their predicted band structure,¹⁴ while Lemay et al. were able to map individual wave functions of CNTs.¹⁵ These breakthroughs were possible because the tunneling current in STM can be measured simultaneously as a function of both energy and location on the sample. One way to achieve this is by using the so-called current imaging tunneling spectroscopy (CITS) mode, during which in each pixel of the CITS image the scanning STM tip acquires a tunneling current vs voltage (STS) curve and stores it together

with the topographic information. Using CITS data, we can obtain local tunneling conductance maps of the sample by plotting the derivative of the current (dI/dV) as a function of the tip–sample bias voltage. Among other examples, it has been applied in mapping the local photovoltaic performance of organic solar cells¹⁶ and in mapping the charge inhomogeneity of SiO_2 supported graphene.¹⁷ However, the full potential of STM as a tool in mapping the electronic properties of functionalized CNT has not been exploited yet. Direct STM and CITS measurements could yield more insight into the extent and nature of sidewall functionalization as opposed to other methods of visualizing functionalized sites.¹⁸ One key difficulty in achieving this is sample stability.

In the case of STM, as with any high resolution microscopy tool, good mechanical stability of the sample is of paramount importance to obtain reliable measurements. Because of the presence of functional groups on the tube surface, the contact area with the substrate decreases, and this leads to a weakening of the overall force (e.g., van der Waals) which anchors the tubes to the support. The metal tip of the STM can exert considerable force, mainly electrostatic in nature, on the tubes,^{19,20} and it can move the CNT in the fast scan direction and can effectively “clean out” the scan area of the tubes we would want to investigate (Figure 1). This is illustrated in Figure 1b, where we show an AFM image of a $20 \times 20 \mu\text{m}^2$ area previously scanned by STM. After only three passes over the same area, practically all of the CNTs have been brushed to the sides. The

Received: September 17, 2010

Revised: January 18, 2011

Published: February 08, 2011

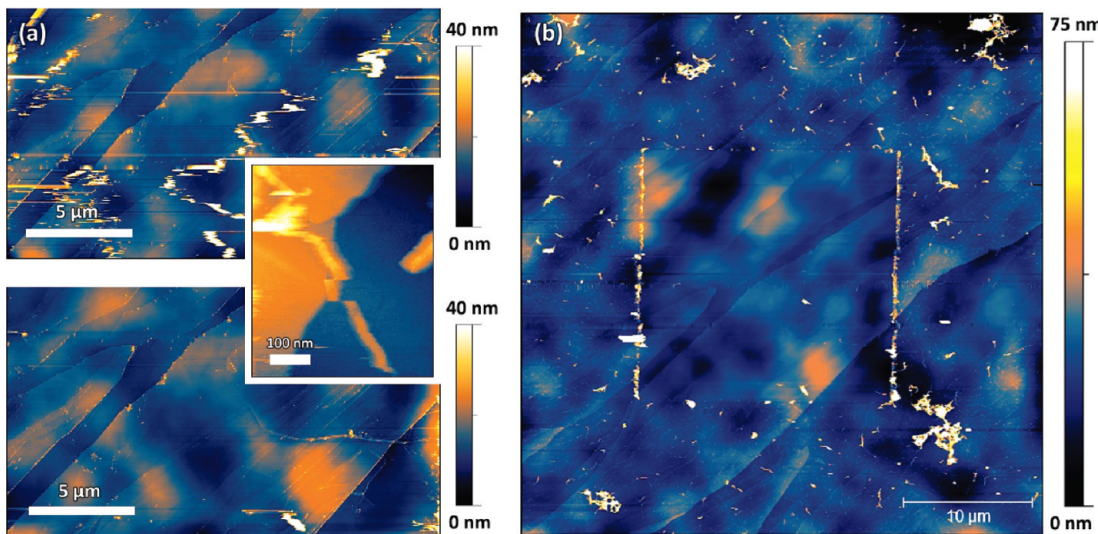


Figure 1. (a) Successive STM images (top and bottom) of a region on HOPG containing functionalized CNTs, showing that nanotubes can be swept away by the STM tip. Extensive movement of the CNT can be observed on the top image. The nanotube movement is also evident in the inset, where a single CNT shifts position during scanning and shifts back to its original position after a few scan lines. (b) Tapping mode AFM image of functionalized CNTs on a HOPG surface measured in a region where the STM tip was previously scanned (Figure 1a). The AFM image is taken after the third STM scan, and it can be seen clearly that the CNTs have been swept to the sides and out of the STM scan area. STM scanning was performed using 300 pA current set point and 100 mV bias voltage. The fast scan direction is horizontal.

inset in Figure 1 shows how, during scanning of the STM tip, a nanotube can move to the side, returning to its original position after a few scan lines. Evidence of such tube movement is also present in the literature.^{18,21–23} While this problem seems to be less critical in the case of lightly functionalized tubes²⁴ and/or if the measurement is performed in UHV,^{25–28} it makes imaging such CNTs a challenge. One way around this problem is to immobilize the nanotubes, for example by binding the tubes to the substrate via strong chemical bonds. A good example for such an approach is the work of Zhang et al.,²² where they have used Au–S chemistry to anchor sulfur containing functional groups on the nanotubes to the Au substrate, effectively immobilizing them. However, this method is not applicable in all cases because of the need to have chemical binding between the nanotubes and substrate. Furthermore, the chemical bond may perturb the tube electronic structure.²² Here we present a method to immobilize CNTs on a graphitic support, which provides a sample that is stable enough to allow reproducible CITS measurements and is a well-studied CNT-support system.

METHODS

The composite presented here is a buckypaper obtained by mixing the functionalized CNT with commercially available exfoliated graphite in isopropyl alcohol by ultrasonic stirring. The as obtained suspension was filtered through a polycarbonate membrane filter (200 nm pore size) and left to dry. Pieces from this buckypaper were cut out and placed on the STM sample holder, and electrical contact to the buckypaper was made by carbon colloid paste.

A Multimode III SPM (Veeco) was operated in the CITS mode to acquire the STM images under ambient conditions and room temperature. The STS data was extracted from the raw CITS files and processed separately using Scilab (www.scilab.org) for easy manipulation and extraction of individual STS curves. All the STM images and STS curves presented here were obtained using the same Pt/Ir STM probe. Tips were

mechanically cut from Pt/Ir (80:20) wire and were used for characterization only if they produced reproducible STS spectra and atomic resolution on graphite. Atomic resolution images on the nanotubes were acquired using 500 pA tunneling current and 100 mV tip–sample bias voltage. STM topography and CITS images were acquired using 300 pA tunneling current and 300 mV bias voltage.

TEM measurements were done using a Philips CM20 microscope operated at 200 keV.

Raman spectra were taken on a Renishaw 1000 MB microscope system with 785 nm exciting laser line. Attenuated total reflection (ATR) spectra were acquired by a Bruker Tensor 27 FTIR instrument using a single-bounce germanium ATR setup.

RESULTS AND DISCUSSION

Multiwalled CNTs used in this study have been prepared by chemical vapor deposition of acetylene over alumina supported Co/Fe catalyst.²⁹ The as obtained nanotubes were subjected to a purification treatment, which was carried out in two steps. First, support and metals were dissolved in concentrated HF (38 wt %) resulting in nanotubes contaminated by amorphous carbon. In the second step, the amorphous carbon was eliminated by the KMnO₄/H₂SO₄ aq. procedure.³⁰ The nanotubes obtained this way are considered to be the “pristine” sample in our study, the functionalization of which was done in a three-step process reported elsewhere.³¹ Briefly, in the first step the pristine CNTs were treated in H₂SO₄/HNO₃ (3:1) mixture for 24 h at room temperature and then stirred overnight in SOCl₂, followed by stirring in diaminopropane for 24 h. This is a typical sequence of defect functionalization: strong oxidation in the first step (due to HNO₃/H₂SO₄ and KMnO₄ during purification), besides eliminating some impurity carbon phases, induces defects on the nanotube walls,³² attaches –OH and –COOH groups to these defects on the CNT outer wall and the tube ends, and in addition causes an overall p-doping of the nanotube π-electron system^{33,34} analogous to intercalated graphite nitrate.³⁵ The

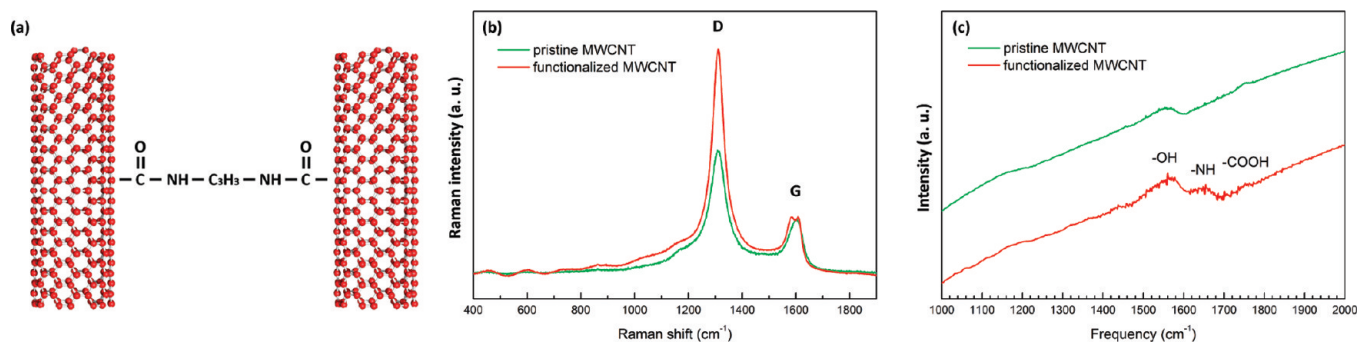


Figure 2. (a) MWCNTs interconnected by diaminopropane. (b) Raman spectra of the starting CNT material and of the functionalized sample. The spectra are normalized to the G peak intensity. (c) ATR-IR spectra showing peaks corresponding to $-\text{OH}$ and $-\text{COOH}$ groups (1720 cm^{-1}) in both the pristine and functionalized samples and a signature of $-\text{NH}$ (1630 cm^{-1}) in the functionalized sample.

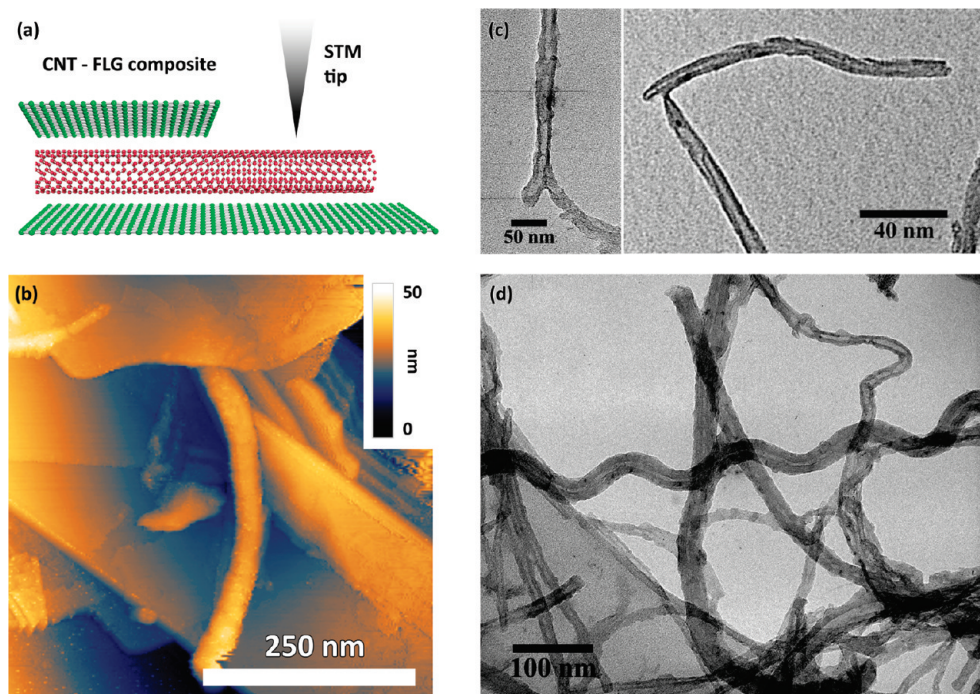


Figure 3. (a) Illustration of the CNT–FLG composite and the STM measurement. (b) STM image of a functionalized CNT sticking out from beneath a FLG layer, also seen in Figure 4d. (c) and (d) TEM images of the functionalized CNT. The surface of the tubes is irregular, and some tubes are interconnected as seen in (c).

defect formation also affects the π -electrons: it converts carbon atoms from sp^2 into sp^3 hybrid state and in this way disrupts the conjugated electron system responsible for conductivity. The following two steps do not involve the tube wall and thus the π -electron system anymore; instead, the second step converts the $-\text{COOH}$ side groups into $-\text{COCl}$, and the third produces a peptide link on the two ends of the diaminopropane, thereby connecting two carboxylic groups. The two carboxylic groups can be either on the same nanotube or on adjacent ones, in the latter case forming covalently interconnected MWCNTs as illustrated in Figure 2a. The TEM image in Figure 3c is also in accordance with the interconnected nanotube model. The increase in defect concentration by the oxidation step manifests itself in the Raman spectra, the D peak intensity increasing relative to the G peak ($I_{\text{D}}/I_{\text{G}}$)³³ (Figure 2b). Attenuated total reflectance infrared (ATR-IR) spectra of the pristine sample show some signs of OH groups, which are most probably of extrinsic origin (solvent

or atmospheric water residues). The spectra of the functionalized samples contain the N–H bending vibration at $\sim 1630 \text{ cm}^{-1}$, indicating the presence of the amine group. The carboxyl vibration around 1720 cm^{-1} is present in both pristine and functionalized samples, indicating that the conversion to $-\text{COCl}$ groups in the second step was not complete.

The concentration of $-\text{COOH}$ groups following acid treatment in commercially available SWNT samples was estimated by Hu et al.³⁶ to be between 1 and 3%. Assuming that the reaction sequence outlined above involves mainly the outer surface of a MWNT, this can be taken as an upper limit because the large diameter of the outer tube implies less reactivity. In the second and third steps, the number of functional groups attached to the nanotubes remains constant. The cross-linked carbon nanotubes, which are partially formed in the reactions described above, are an interesting avenue in improving the mechanical and electrical transport properties of nanotube networks,^{37,38} and

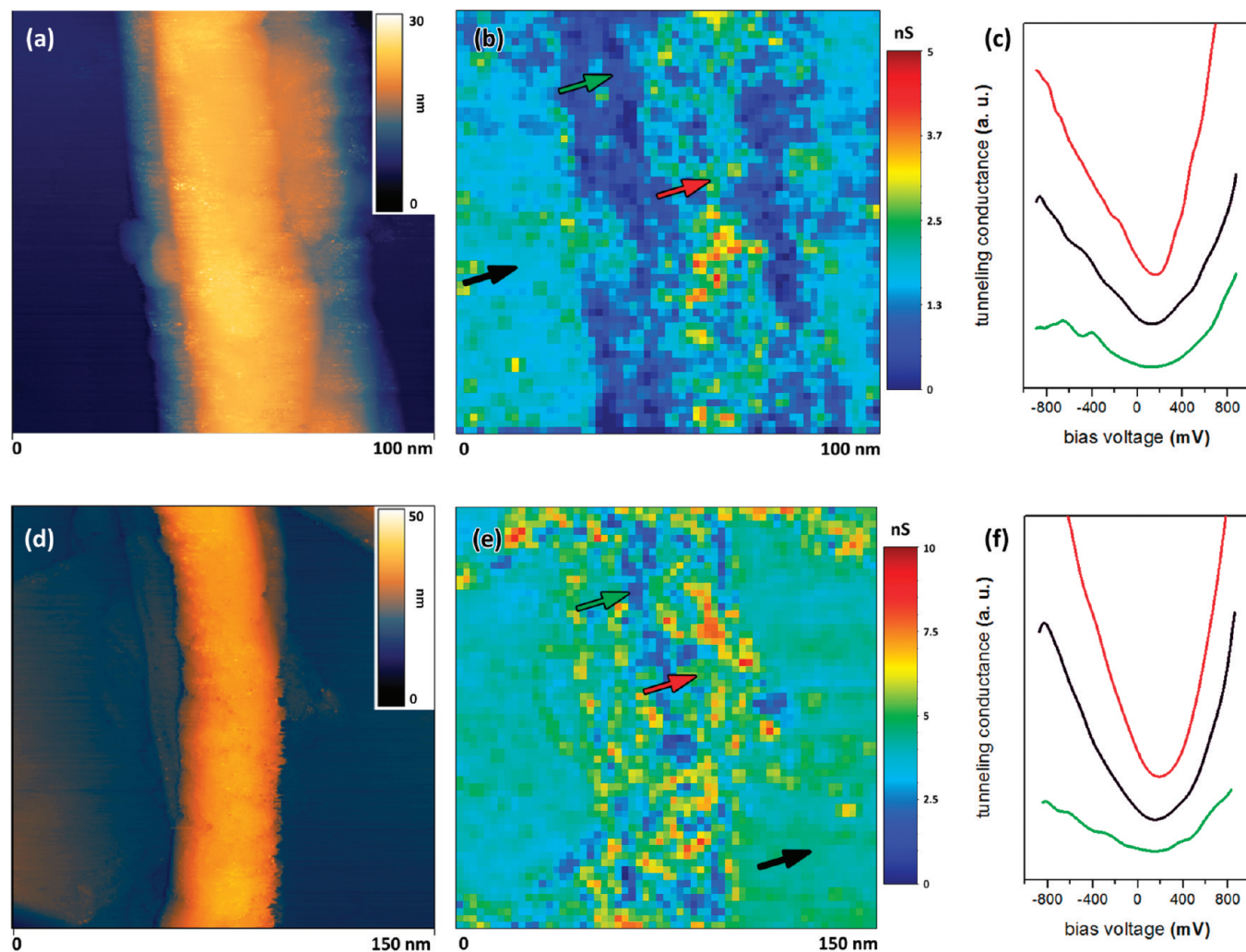


Figure 4. (a), (d) STM images and (b), (e) tunneling conductance maps of functionalized nanotubes extending from below a FLG clamping layer (conductance units are in nanosiemens). (a) shows a bundle of three nanotubes, which are possibly cross-linked by functional groups. In (c) and (f) we show dI/dV spectra from the regions marked by arrows of the same color as in (b) and (e), respectively. The spectra are selected from three regions: the FLG substrate (black) and regions of low (green) and high conductance (red) on the nanotube. The spectra are displaced vertically for ease of comparison. The tunneling conductance maps are displayed at -160 mV bias voltage.

functionalization schemes similar to our own have been studied.^{6,39} Here we report for the first time atomic resolution STM and CITS measurements on such CNTs.

The immobilization of the functionalized CNTs is done by sandwiching them between few-layer graphite (FLG) flakes in a CNT–FLG composite, in buckypaper form (Figure 3a, b). The buckypaper is obtained by mixing CNT and FLG suspended in isopropyl alcohol, using ultrasonic agitation and subsequent filtering on a polycarbonate membrane. The nanocomposite has regions on its surface where functionalized CNTs stick out from beneath a FLG layer. Figure 3b shows an STM image of such a region. Here the movement of the nanotube is restricted by the clamping FLG layer and provides a location suitable for stable and reproducible STM and CITS measurements. This particular composite is advantageous, because graphite and MWCNTs have nearly the same work function,⁴⁰ thus, no significant charge transfer is expected between the two components.

STM images of a bundle of three functionalized nanotubes and a single tube can be seen in Figure 4a and Figure 4d, while in Figure 4b, e we present a map of the simultaneously acquired

local tunneling conductance on these tubes. We obtained this map from the CITS image by taking the first derivative of the STS curves and displaying the conductance value at -160 mV bias voltage. We can observe on the same image the different conductance of the graphite support and of the nanotubes. Such dI/dV tunneling conductance maps are qualitatively proportional to the nanotube local density of states (LDOS). At a first glance the dI/dV map on the nanotube surface shows regions of high and low conductance. Comparing the dI/dV curves from such selected regions, we can see some similarities and some differences in the spectra. The curves from the high conductance regions (red arrow and curve) and the substrate (black arrow and curve) are similar and have a typical graphitic shape, with monotonically increasing conductance that is symmetrical with respect to the LDOS minimum. Measuring a graphitic dI/dV signal on multiwalled CNTs is a reasonable expectation, because at the large tube diameters in this sample (~ 15 nm) the Van Hove singularities are very close together and get smoothed out due to the spread of the Fermi function at 300 K and due to disorder effects.⁴¹ The minimum of LDOS, which occurs because

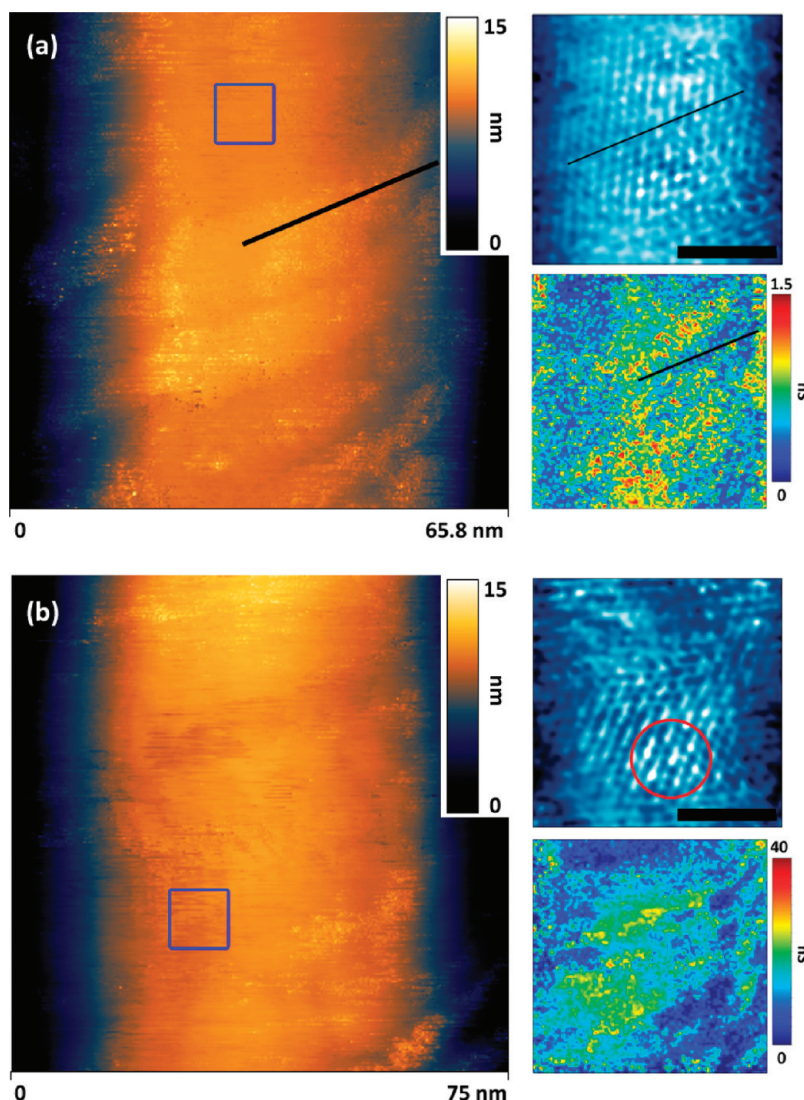


Figure 5. (a), (b) STM images of two different regions of the functionalized CNT shown in Figure 4d. Panels to the right of the topography images show zoomed in, lattice resolved images obtained in the regions marked by blue squares and tunneling conductance maps obtained simultaneously with the topography, displayed at -225 mV bias voltage. Functionalized regions show up as protrusions on the nanotube surface and as low conductance areas in the conductance maps. Black lines mark the zigzag direction on the atomic resolution image and one of the “bands”, where functionalization is more pronounced. The functionalized regions follow the zigzag direction. The superstructure patterns on the atomic lattice are a sign of defect scattering (marked by the circle).

of the vanishing electron states at the K points, is shifted slightly to positive tip–sample bias voltages. This means that the chemical potential is shifted away from its equilibrium position, i.e., that the sample is p-doped. It has been shown that nitric and sulfuric acid can have a strong, p-doping effect on CNTs.^{33,34} In our case, acid molecules adsorbed on the nanotube surface are a result of the purification treatment. These molecules donate a positive charge to the carbon lattice, which becomes delocalized over the π -electron system. This process leads to a “global” p-doping of the nanotubes and has been measured previously by optical reflectivity and thermopower measurements.^{33,34} But the true power of CITS measurements comes from the local information it provides. Thus, examining the conductance maps further, we can see regions with lower conductance than the support or other regions on the tubes (green arrow and curve). dI/dV curves in these regions have a much less well-defined minimum and are highly asymmetrical in places. We attributed

these types of curves to defective and/or intensely functionalized regions of the CNTs, where the low conductance values arise from the destruction of the conjugated π -electron system.⁴² This conclusion is also supported by the TEM images showing damaged graphitic layers of the tubes (Figure 3c, d).

The STM topography of these tubes also shows a rough surface, which is typical of highly defective and functionalized CNT, where the functional groups usually appear as protrusions on the nanotube surface.^{22,24} Figure 5a and 5b show two distinct STM topography images of a functionalized CNT. Comparing the conductance maps with the topography, we observe a degree of correlation between the low conductance regions and the protrusions on the surface. Especially in Figure 5a, bands of protrusions coincide with bands of low conductance in the corresponding dI/dV map. Furthermore, it was not possible to obtain atomic resolution images on the low conductance regions, only on the regions with high conductance. In addition to the

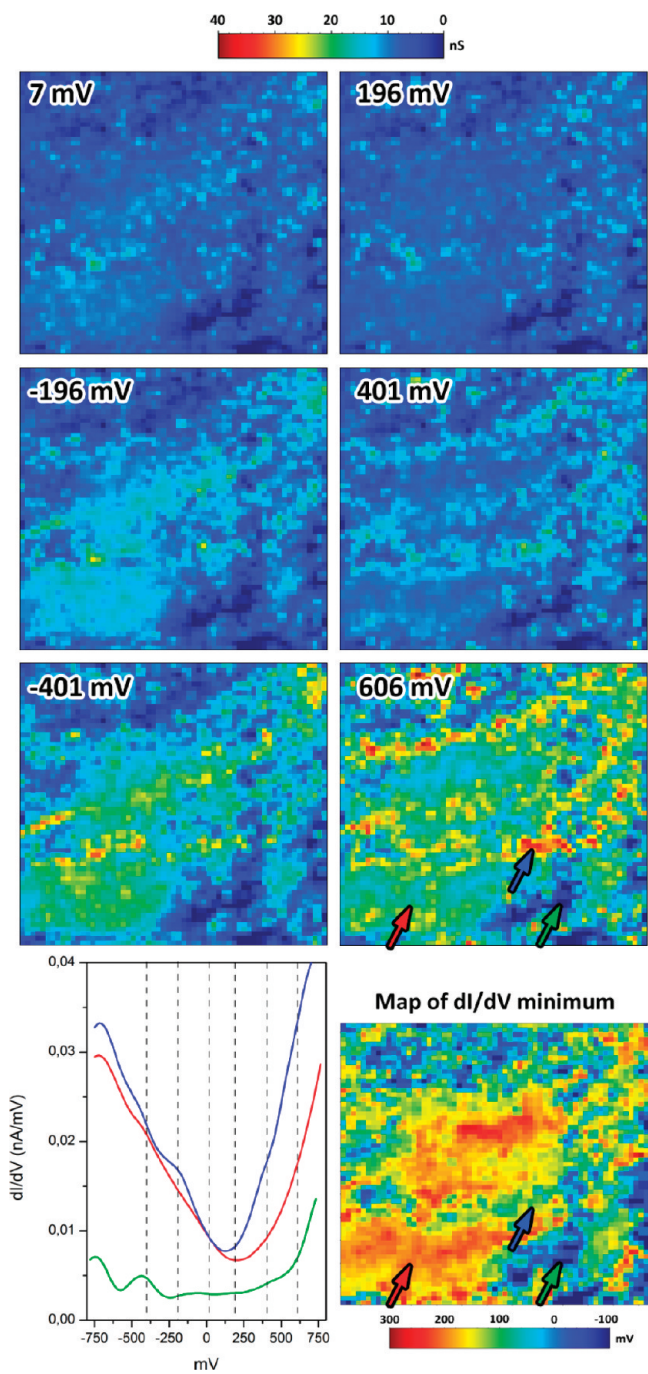


Figure 6. Tunneling conductance maps of the nanotube region seen in Figure 5b, with selected dI/dV curves. The bias voltages at which the maps were plotted are marked by dashed lines. Atomic resolution was achieved in the region marked by the red arrow. The low conductance regions show similar dI/dV curves as the ones seen in Figure 4 (green). (The dI/dV maps are 75×75 nm in size.) Lower right: map of the dI/dV minimum in the same region as the conductance map; the bias voltage value for the dI/dV minimum is displayed on a color scale. Colored arrows show the positions where the respective dI/dV curves were taken.

graphitic dI/dV curves, this suggests that the regions with high conductance are mostly free of defects and functional groups. Here the atomic lattice shows a typical superstructure pattern, a hallmark of electron scattering between two nonequivalent K

points in the Brillouin zone.^{24,28,43} As these superstructure patterns can extend to a few nanometers from the defect site producing them,⁴³ it is fair to say that they are due to scattering taking place on the defects created during oxidation and functionalization. If we compare the atomic resolution images with the functionalized bands, we find that these follow the zigzag direction along the nanotube circumference. To date, only a few such STM studies are available which show the correlation between crystallographic direction and functionalization, for example on fluorinated CNTs.²⁸ These measurements provide experimental evidence that oxidation of CNTs can prefer a specific crystallographic direction, as it was presumed in recent experiments which involved the unzipping of carbon nanotubes to graphene nanoribbons.^{44,45} A similar effect was exploited when cutting oxidized graphene sheets.⁴⁶ Our results strengthen the evidence found in the literature that, when acidic oxidation is involved, etching takes place along the zigzag direction.

In Figure 6 we examine the dI/dV maps of one nanotube in more detail: we show six plots of the tunneling conductance map of the tube shown in Figure 5b at different tip–sample bias voltages. These voltages have been selected to be symmetrical relative to the dI/dV minimum. We can distinguish three regions based on these maps. One region is where atomic resolution could be achieved (marked by a red arrow). Maps of such regions have symmetrical conductance values with respect to the minimum of dI/dV or in other words to the LDOS minimum. Such behavior is graphitic in nature, due to the symmetry in energy of the nanotube bands around the K points. As we have seen before, another region is where the overall conductance is low and no atomic resolution can be achieved. We attribute these changes to heavily functionalized regions (marked with a green arrow). Further inspection of the maps reveals a third region, where the dI/dV maps are asymmetrical; here the tunneling conductance is higher for positive tip–sample bias voltages (blue arrow). The origin of this asymmetry is not clear, but it may be due to impurity states at functionalized or defect sites.^{44,47} Another feature of this dI/dV curve is that its minimum is shifted toward a more negative sample voltage, making this region less p-doped. We can expect such behavior if there is charge asymmetry between the nanotube and the functional group, which leads to a local Coulomb potential and therefore to a shift in energy of the nanotube bands. In Figure 6 we plot a map of the LDOS minimum on the nanotube by displaying the bias voltage value for the dI/dV minimum on a color scale. From this map we can see that the mostly functional group free regions are heavily p-doped, with a Fermi level shift of around 0.25 eV. This is the global doping level of the sample, and as we discussed earlier it arises due to acid molecule adsorption. The map of LDOS minima correlates nicely with the conductance map showing the places of asymmetric dI/dV curves attributed to functionalized sites (blue arrows in Figure 6). We have to mention that the interpretation of this map is not straightforward in the low conductance regions, where the sp^2 carbon lattice is heavily damaged and the electronic structure of the surface is unknown.

CONCLUSIONS

The CNT immobilization technique presented here is widely applicable to any type of functionalized nanotube and provides a well-studied CNT-support system for STM measurements. We have shown for the first time that oxidation and subsequent functionalization have a preference of advancing along the zigzag

crystallographic direction on large diameter multiwalled CNTs. Our measurements illustrate clearly the kind of advantage energy resolved maps can give, namely to spot sample features that are not apparent from STM topography maps and to provide information on local functionalization and doping. Furthermore, this measurement technique allows certain “in situ” studies that could not be performed otherwise, for example, to examine the topography and energy resolved behavior of functionalized CNTs, while being exposed to different gas or vapor environments.¹⁰ This may lead to a better understanding of the adsorption processes and the electronic structure variations involved in gas sensing with functionalized nanotube networks.

■ AUTHOR INFORMATION

Corresponding Author

*E-mail nemes@mfa.kfki.hu.

■ ACKNOWLEDGMENT

The work was financially supported by OTKA-NKTH projects 67793, 67851, 75813, and T049182. One of the authors (Z.E.H.) is a grantee of a Bolyai János Scholarship.

■ REFERENCES

- (1) Burghard, M. *Surf. Sci. Rep.* **2005**, *58*, 1–109.
- (2) Balasubramanian, K.; Burghard, M. *Small* **2005**, *1*, 180–92.
- (3) Tasis, D.; Tagmatarchis, N.; Bianco, A.; Prato, M. *Chem. Rev.* **2006**, *106*, 1105–36.
- (4) Park, H.; Zhao, J.; Lu, J. P. *Nanotechnology* **2005**, *16*, 635–638.
- (5) Strano, M. S.; Dyke, C. A.; Usrey, M. L.; Barone, P. W.; Allen, M. J.; Shan, H.; Kittrell, C.; Hauge, R. H.; Tour, J. M.; Smalley, R. E. *Science* **2003**, *301*, 1519–22.
- (6) Hu, H.; Zhao, B.; Hamon, M. A.; Kamaras, K.; Itkis, M. E.; Haddon, R. C. *J. Am. Chem. Soc.* **2003**, *125*, 14893–900.
- (7) López-Bezanilla, A.; Triozon, F.; Latil, S.; Blase, X.; Roche, S. *Nano Lett.* **2009**, *9*, 940–4.
- (8) Sainsbury, T.; Erickson, K.; Okawa, D.; Zonte, C. S.; Fréchet, J. M.; Zettl, A. *Chem. Mater.* **2010**, *22*, 2164–2171.
- (9) Eitan, A.; Jiang, K.; Dukes, D.; Andrews, R.; Schadler, L. S. *Chem. Mater.* **2003**, *15*, 3198–3201.
- (10) Horváth, Z. E.; Koós, A. A.; Kertész, K.; Molnár, G.; Vértesy, G.; Bein, M. C.; Frigyes, T.; Mészáros, Z.; Gyulai, J.; Biró, L. P. *Appl. Phys. A: Mater. Sci. Process.* **2008**, *93*, 495–504.
- (11) Klinke, C.; Hannon, J. B.; Afzali, A.; Avouris, P. *Nano Lett.* **2006**, *6*, 906–10.
- (12) Yun, Y.; Dong, Z.; Shanov, V.; Heineman, W.; Halsall, H.; Bhattacharya, A.; Confrati, L.; Narayan, R.; Ball, W.; Schulz, M. *Nano Today* **2007**, *2*, 30–37.
- (13) Zhang, Y.; Kanungo, M.; Ho, A. J.; Freimuth, P.; van Der Lelie, D.; Chen, M.; Khamis, S. M.; Datta, S. S.; Johnson, A. T.; Misewich, J. A.; Wong, S. S. *Nano Lett.* **2007**, *7*, 3086–91.
- (14) Wildöer, J. W.; Venema, L. C.; Rinzler, A. G.; Smalley, R. E.; Dekker, C. *Nature* **1998**, *391*, 59.
- (15) Lemay, S. G.; Janssen, J. W.; van Den Hout, M.; Mooij, M.; Bronikowski, M. J.; Willis, P. A.; Smalley, R. E.; Kouwenhoven, L. P.; Dekker, C. *Nature* **2001**, *412*, 617–20.
- (16) Maturová, K.; Janssen, R. A.; Kemerink, M. *ACS Nano* **2010**, *4*, 1385–92.
- (17) Deshpande, A.; Bao, W.; Miao, F.; Lau, C. N.; LeRoy, B. J. *Phys. Rev. B* **2009**, *79*, 205411.
- (18) Zhang, L.; Zhang, J.; Schmandt, N.; Cratty, J.; Khabashesk, V. N.; Kelly, K. F.; Barron, A. R. *Chem. Commun.* **2005**, 5429–31.
- (19) Curran, S.; Carroll, D. L.; Ajayan, P. M.; Redlich, P.; Roth, S.; Rühle, M.; Blau, W. *Adv. Mater.* **1998**, *10*, 311–313.
- (20) Biró, L. P.; Gyulai, J.; Lambin, P.; B.Nagy, J.; Lazarescu, S.; Márk, G. I.; Fonseca, A.; Surján, P. R.; Szekeres, Z.; Thiry, P. A.; Lucas, A. A. *Carbon* **1998**, *36*, 689–696.
- (21) Kónya, Z.; Vesselenyi, I.; Niesz, K.; Kukovecz, A.; Demortier, A.; Fonseca, A.; Delhalles, J.; Mekhalif, Z.; B.Nagy, J.; Koós, A. A.; Osváth, Z.; Kocsonya, A.; Biró, L. P.; Kiricsi, I. *Chem. Phys. Lett.* **2002**, *360*, 429–435.
- (22) Zhang, J.; Zhang, L.; Khabashesk, V. N.; Barron, A. R.; Kelly, K. F. *J. Phys. Chem. C* **2008**, *112*, 12321–12325.
- (23) Osváth, Z.; Koós, A. A.; Grobert, N.; Vértesy, Z.; Horváth, Z. E.; Biró, L. P. *J. Nanosci. Nanotechnol.* **2009**, *9*, 6139–6143.
- (24) Nemes-Incze, P.; Tapaszto, L.; Darabont, A.; Lambin, P.; Biró, L. P. *Carbon* **2009**, *47*, 764–768.
- (25) Graupner, R.; Abraham, J.; Wunderlich, D.; Venczelová, A.; Lauffer, P.; Röhrl, J.; Hundhausen, M.; Ley, L.; Hirsch, A. *J. Am. Chem. Soc.* **2006**, *128*, 6683–9.
- (26) Bonifazi, D.; Nacci, C.; Marega, R.; Campidelli, S.; Ceballos, G.; Modesti, S.; Meneghetti, M.; Prato, M. *Nano Lett.* **2006**, *6*, 1408–14.
- (27) Lauffer, P.; Jung, A.; Graupner, R.; Hirsch, A.; Ley, L. *Phys. Status Solidi B* **2006**, *243*, 3213–3216.
- (28) Kelly, K. F.; Chiang, I. W.; Mickelson, E. T.; Hauge, R. H.; Margrave, J. L.; Wang, X.; Scuseria, G. E.; Radloff, C.; Halas, N. J. *Chem. Phys. Lett.* **1999**, *313*, 445–450.
- (29) Willem, I.; Kónya, Z.; Colomer, J. F.; Tendeloo, G. V.; Nagaraju, N.; Fonseca, A.; Nagy, J. B. *Chem. Phys. Lett.* **2000**, *317*, 71–76.
- (30) Hernadi, K.; Fonseca, A.; Nagy, J. B.; Bemaerts, D.; Fudala, A.; Lucas, A. A. *Zeolites* **1996**, *17*, 416–423.
- (31) Kiricsi, I.; Kónya, Z.; Niesz, K.; Koós, A. A.; Biro, L. P. In *Nanotechnology*; Vajtai, R.; Aymerich, X.; Kish, L. B.; Rubio, A. *Proc. SPIE—Int. Soc. Opt. Eng.* **2003**, *5118*, 280–287.
- (32) Monthoux, M.; Smith, B. W.; Berteaux, B.; Claye, A.; Fischer, J. E.; Luzzi, D. E. *Carbon* **2001**, *39*, 1251–1272.
- (33) Zhou, W.; Vavro, J.; Nemes, N.; Fischer, J.; Borondics, F.; Kamarás, K.; Tanner, D. *Phys. Rev. B* **2005**, *71*, 205423.
- (34) Kamarás, K.; Pekker, Á.; Botka, B.; Hu, H.; Niyogi, S.; Itkis, M. E.; Haddon, R. C. *Phys. Status Solidi B* **2010**, *247*, 2754–2757.
- (35) Forsman, W. C.; Vogel, F. L.; Carl, D. E.; Hoffman, J. *Carbon* **1978**, *16*, 269–271.
- (36) Hu, H.; Bhowmik, P.; Zhao, B.; Hamon, M. A.; Itkis, M. E.; Haddon, R. C. *Chem. Phys. Lett.* **2001**, *345*, 25–28.
- (37) Pugno, N. M. *Mater. Today* **2010**, *13*, 40–43.
- (38) Cha, S. I.; Kim, K. T.; Lee, K. H.; Mo, C. B.; Jeong, Y. J.; Hong, S. H. *Carbon* **2008**, *46*, 482–488.
- (39) Chiu, P. W.; Duesberg, G. S.; Dettlaff-Weglikowska, U.; Roth, S. *Appl. Phys. Lett.* **2002**, *80*, 3811.
- (40) Shiraishi, M.; Ata, M. *Carbon* **2001**, *39*, 1913–1917.
- (41) Hügle, S.; Egger, R. *Phys. Rev. B* **2002**, *66*, 193311.
- (42) Kamarás, K.; Itkis, M. E.; Hu, H.; Zhao, B.; Haddon, R. C. *Science* **2003**, *301*, 1501.
- (43) Tapaszto, L.; Nemes-Incze, P.; Osváth, Z.; Darabont, A.; Lambin, P.; Biró, L. P. *Phys. Rev. B* **2006**, *74*, 235422.
- (44) Kosynkin, D. V.; Higginbotham, A. L.; Sinitskii, A.; Lomeda, J. R.; Dimiev, A.; Price, B. K.; Tour, J. M. *Nature* **2009**, *458*, 872–6.
- (45) Paiva, M. C.; Xu, W.; Fernanda Proençā, M.; Novais, R. M.; Lægsgaard, E.; Besenbacher, F. *Nano Lett.* **2010**, *10*, 1764–1768.
- (46) Fujii, S.; Enoki, T. *J. Am. Chem. Soc.* **2010**, *132*, 10034–41.
- (47) Osváth, Z.; Vértesy, G.; Tapaszto, L.; Wéber, F.; Horváth, Z.; Gyulai, J.; Biró, L. P. *Phys. Rev. B* **2005**, *72*, 045429.